Chapter 4

Dynamics of A Rotating Sunspot[1]

4.1 Introduction

Sunspots that exhibit some degrees of rotational motion around its own vertical axis are not rare in solar observations (Knoška, 1975). Many authors (e.g., Tokman & Bellan , 2002) suggested that some solar eruptive events, such as solar flares and coronal mass ejections, are correlated with rotational and sheared motions of sunspots. Recently, Brown et al. (2003) studied several rotating sunspots observed by *TRACE*, and calculated the total magnetic helicity and energy generated by the sunspot rotation. They found that the sunspot rotation can twist coronal loops and trigger solar flares. On the other hand, many authors investigated the origin of the magnetic twists observed in vector magnetograms and coronal loop structures, and some explanations have been proposed including the solar differential rotation, surface motions and turbulent motions in solar convection zone (see review by Canfield & Pevtsov, 2000). More recently, based on analysis of 22 bipolar solar active regions, López Fuentes et al. (2003) proposed that the magnetic deformation may result from large-scale vortical flows in the solar convection zone and the photosphere or in subphotospheric layers. Therefore, it is of great importance and interest to investigate the subsurface structures and dynamics of rotating sunspots. These studies may shed light on

[1]Most part of this chapter was published in the Astrophysical Journal (Zhao & Kosovichev, 2003b)

physical conditions in the solar convection zone, the interaction between convective motions and magnetic structures of sunspots, the formation of magnetic twists, the energy storage for solar eruptions and many other interesting topics of solar physics.

In this chapter, we apply the method of time-distance helioseismology to a fast rotating sunspot observed by *SOHO*/MDI in August 2000, and present maps of subsurface flows and sound-speed variations. We demonstrate that the structural twist of magnetic flux exists below the photosphere, as argued by Leka, Canfield, & McClymont (1996); and we present the subsurface vortical flows which may further twist the magnetic flux and store more magnetic energy and magnetic helicity required by solar eruptions. In this chapter, we also show some error analysis and do the mask experiment to test the reliability of our inversion results.

4.2 Observations

4.2.1 MDI Observations

The full-disk Dopplergrams with one-minute cadence used for our analyses were obtained from *SOHO*/MDI (Scherrer et al., 1995). The spatial resolution is 2 arcsecond, corresponding to 0.12 heliographic degree per CCD pixel.

Active region NOAA 9114 passed through the solar disk from August 4 to August 12, 2000. The movie made from the MDI magnetograms with a temporal interval of 96 minutes from August 6 to August 10 showed in this active region a fast rotating leading large sunspot, and a small satellite sunspot moving closer to the leading sunspot and merging with it on August 8. After the merge the sunspot continued its rotation until August 10. The sunspot's rotation is clearly seen because the larger sunspot is not completely round, but has a protruding feature "A", as marked in Figure 4.1. It shows counter-clockwise rotation around the main sunspot. Although rotation of sunspots is not rare in solar observations, this case of such a rapid and large degree rotation (approximately 200° within 3 days) is rather unusual.

Figure 4.1 shows a magnetogram obtained by *SOHO*/MDI at 16:11UT on August 7. The path of the small sunspot from 00:00UT, August 6 to 08:00UT of August 10

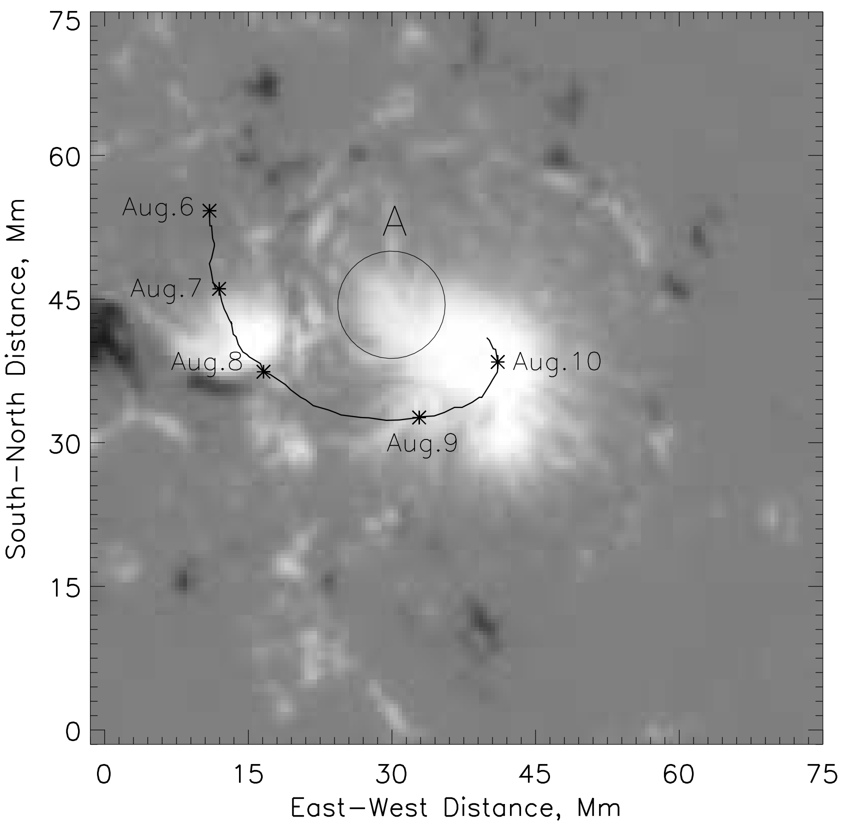

Figure 4.1: Line-of-sight magnetogram obtained by *SOHO*/MDI at 16:11UT of August 7, 2000. The solid line shows the path of the small sunspot from 00:00UT August 6 to 08:00UT August 10. Asterisks mark the 00:00UT of August 6 through August 10 respectively. The protruding part from the larger sunspot in the circle is marked as feature "A". The magnetic field strength ranges from -1100 to 1600 Gauss.

is plotted as a solid line in Figure 4.1, with asterisks marking 00:00UT of every day from August 6 to 10. The small sunspot moved along a curve rather than a straight line before the merge, and after merging with the larger sunspot, it rotated together with this sunspot.

4.2.2 Observations by *TRACE* and Mees Observatory

The *Transition Region and Coronal Explorer (TRACE)* (Schrijver et al., 1999) also gave continuous observation of this interesting event from Aug. 8 to Aug. 10 both in white light and in 171Å. *TRACE* has a spatial resolution of 0.5 arcsec, better than SOHO/MDI full disk observation. Figure 4.2 shows an image of *TRACE* 171Å observation of this active region, with the contours showing the boundaries of the penumbra and umbra of this sunspot. The magnetic loops above the sunspot shows a so-called "fan" structure, which means that the magnetic loops deviate from their potential field.

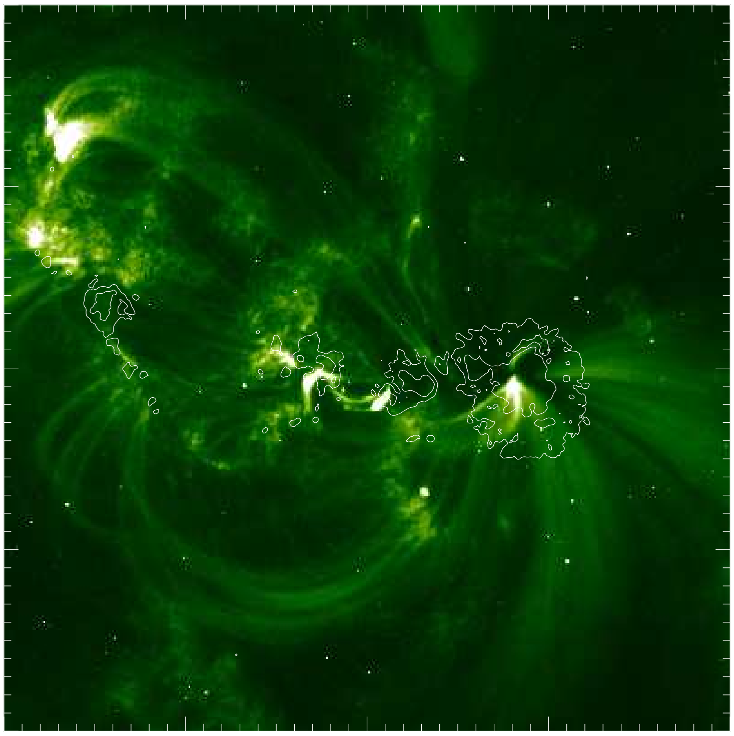

Figure 4.2: *TRACE* observation of this active region. The image is 171Å observation by *TRACE*, and the contour is from white light observation showing the boundary of umbra and penumbra of the sunspot. The scale of this graph is 138 Mm $\times$ 138 Mm.

The Imaging Vector Magnetogram (IVM) at Mees Solar Observatory (Mickey et al., 1996) observed the transverse magnetic field of this active region. Figure 4.3 shows the transverse magnetic field overlapping white light image of the sunspot. Obvious counter-clockwise transverse magnetic field twists deviating away from the potential field can be seen on the right hand side of the sunspot's center. The observations of August 7 and 9 also show some twists in transverse magnetic field, but the twists are not so strong as on August 8.

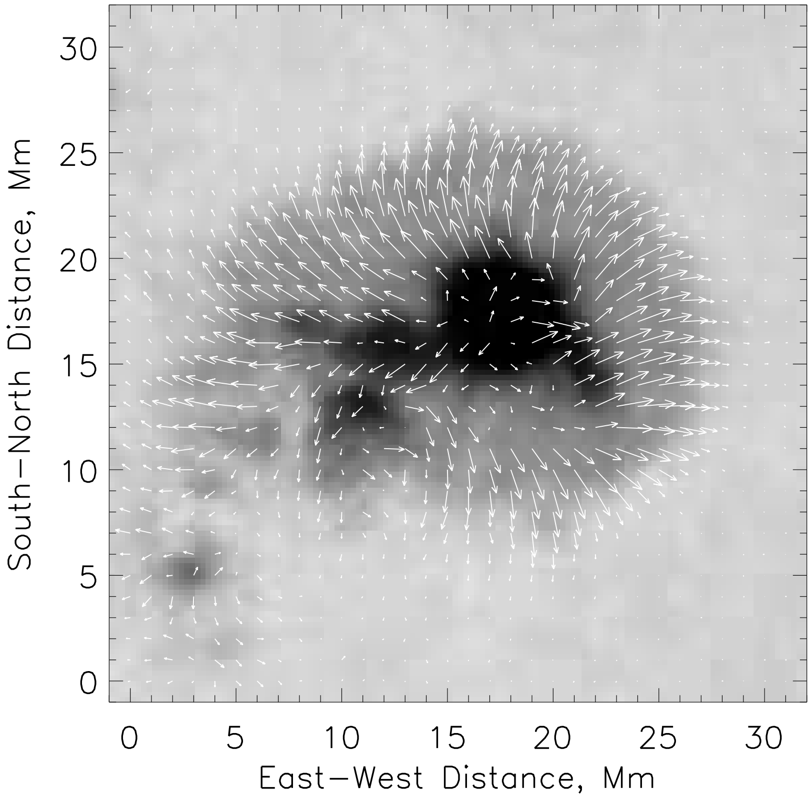

Figure 4.3: Transverse magnetic field, shown by arrows, overlapping the white light image from the Mees Solar Observatory. The longest arrow represents the magnetic strength of 1100 Gauss.

4.2.3 Time-Distance Measurement and Inversion

To perform the time-distance helioseismology measurements with an acceptable signal-to-noise ratio, we select the following two observing periods, both of which last 512 minutes, for our time-distance analyses: 16:20UT August 7 – 00:51UT August 8, 2000 and 04:08UT – 12:39UT August 8, 2000 (for simplicity, we refer to them as August 7 data and August 8 data respectively).

Time-distance measurements and inversions were then performed following the procedures described in Chapter 2. In Chapter 3, we tested the accuracy and convergence of the LSQR algorithm using artificial data, and found that this technique can recover three-dimensional flow structures up to 15 Mm beneath the visible surface. Moreover, in §2.3, we demonstrated the inversion results obtained by LSQR algorithm agree well with the inversion results from Multi-Channel Deconvolution. The results that are to be presented in the following were inverted using LSQR algorithm and MCD technique was employed to ascertain the results.

Here, we present some additional inversion tests for noise-free artificial data to estimate the ability of the LSQR-based inversion technique to measure vortical flows and detect opposite flows within relatively short depth ranges. The upper panels of Figure 4.4 show the original artificial data, with downward and converging counter-clockwise vortical flows at the depth of 0 – 3 Mm, and upward and diverging clockwise flows at the depth of 9 – 12 Mm. The lower panels show the inversion results from the artificial data following the procedure in Chapter 3. We can find that the inversion results reproduce very well the flow patterns of the artificial data, with the correlation coefficient as high as 98.9% for the depth of 0 – 3 Mm, and 94.7% for 9 – 12 Mm.

4.3 Results

4.3.1 Results of Sound Speed Variation

Previous observations have shown that the average sound-speed variation $\delta c/c$ relative to the quiet Sun is mostly positive below the depth of $\sim$4 Mm in active regions (Kosovichev, Duvall, & Scherrer, 2000; Sun et al., 2002). We may assume that the

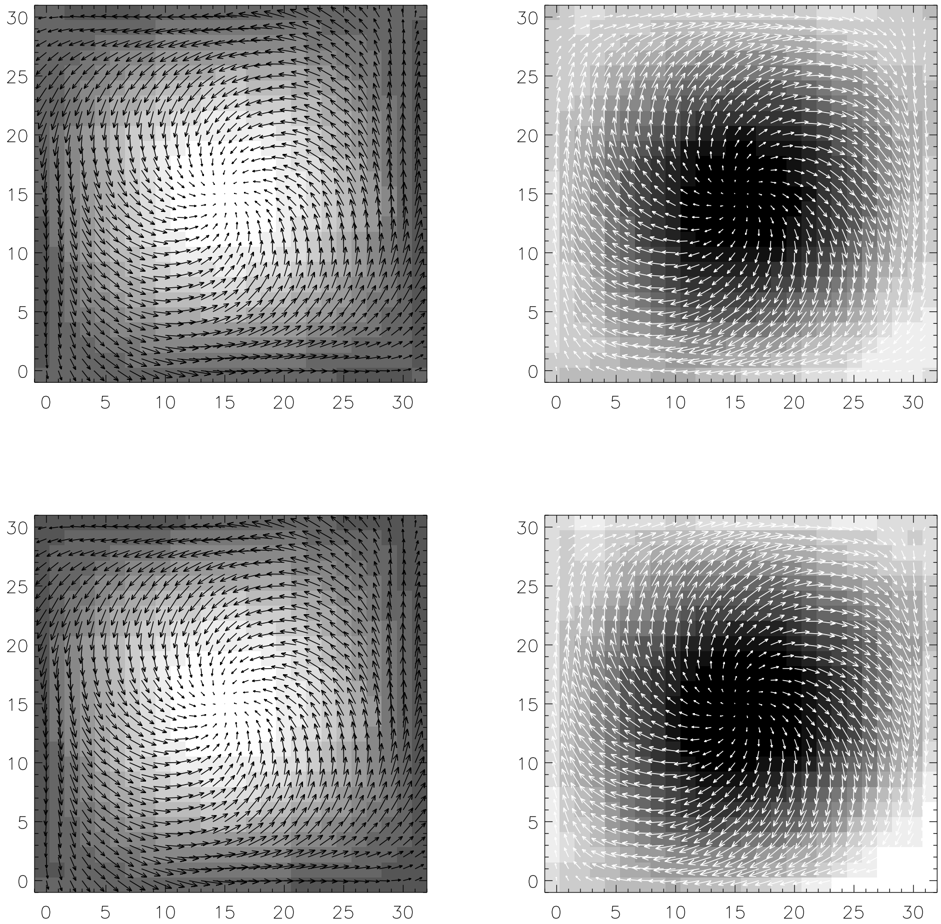

Figure 4.4: Test results from noise-free artificial data. Background images in each graph represent the vertical velocities, with bright as upward flows and gray as downward. Arrows indicate the horizontal flows. The upper two graphs are the artificial data for the depth of 0 – 3 Mm (*left*) and 9 – 12 Mm (*right*) respectively, and the lower two graphs are the inversion results. Scales are arbitrary in these graphs.

horizontal shape of the subsurface sound-speed variation corresponds to the shape of the subsurface magnetic field structure, however, the precise relation between them has not yet been established.

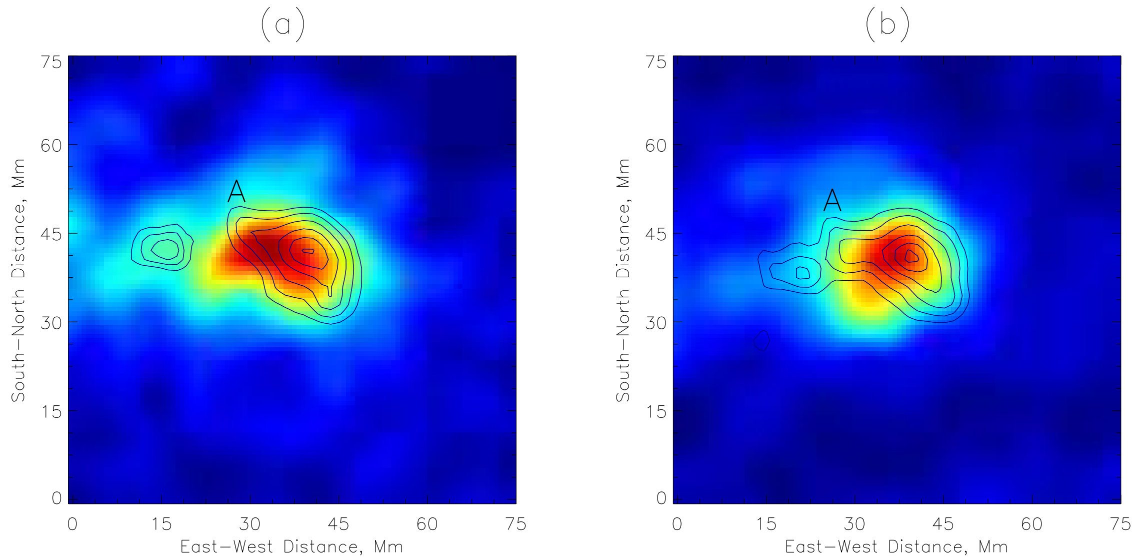

Figure 4.5: Sound-speed variation maps at the depth of 6 Mm (background color images) and the photospheric line-of-sight magnetic field (contour lines) for two observing intervals: a) 16:20UT August 7 – 00:51UT August 8, 2000; b) 04:08UT August 8 – 12:39UT August 8, 2000. The red color corresponds to positive sound-speed variation $\delta c/c$, and the blue one corresponds to negative $\delta c/c$ which ranges from -0.02 to 0.08. The contour levels are 600, 800, 1000, 1200, 1400, 1600 Gauss.

In Figure 4.5a, the background image shows the sound-speed variation structure at the depth of 6 Mm, obtained from the August 7 data. The contour lines in this graph show the line-of-sight magnetic field averaged from all 1-minute cadence magnetograms during the 512-min observation period. Even though the exact correspondence between the photospheric structures and the subsurface sound-speed structures cannot be easily seen, it appears that the subsurface structure is rotated by $\sim 34^\circ$ counter-clockwise with respect to the photospheric sunspot structure. The root of the small sunspot which eventually merged with the larger sunspot is not identified as a separate structure in our data. This may imply that the root of the small satellite sunspot was probably connected to the magnetic flux clusters of the main sunspot deeper than the depth of a few megameters (see also, Kosovichev, Duvall, & Scherrer, 2000).

Figure 4.5b shows the sound-speed variation map and the averaged line-of-sight magnetic field from the August 8 data. In this case, the shape of the sound-speed variation is not in the same good accordance with the shape of the surface magnetic field as in Figure 4.5a. However, the protruding part of the sound-speed structure seems to correspond well to feature "A" on the surface, thus forming an angle of $\sim 45°$ between these features. These observations seem to suggest the existence of the subsurface structural twist of the sunspot in both datasets.

4.3.2 Flow Fields Beneath the Surface

Three-dimensional velocity maps have also been obtained from the August 7 and 8 data. The left panels of Figure 4.6 present the velocity fields at two depth intervals of 0 – 3 and 9 – 12 Mm obtained from the August 7 data, while the right panels show the velocity fields at the same depth intervals for the August 8 data.

In the upper layer (0 – 3 Mm in depth), we find strong converging flows with downdrafts in the sunspot area, as found by Zhao, Kosovichev, & Duvall (2001). Except for the lower left corner (or the southeast part) of the main sunspot, an apparent counter-clockwise vortical flow can be found around the sunspot for both dates August 7 and 8, with stronger vorticity on August 8. This vortex has the same counter-clockwise direction as the sunspot surface rotation. Similar vortical flow patterns are found at the depth of 3 – 5 Mm, which implies that the rotational motions seen at the surface extends to 5 Mm in depth.

In the deeper layer (9 – 12 Mm in depth), we observe that divergent flows with upward flows replace the converging downflows in the sunspot area. A strong clockwise vortex can be seen in the August 8 graph (Figure 4.6d) in and around the sunspot region. The August 7 data (Figure 4.6b) also show this vortex but of a smaller vorticity. It appears that the direction of the vortex seen at this depth is opposite to the surface rotation of the sunspots.

In order to show more clearly the vortical flows in and around the sunspot region, we present in Figure 4.7 the tangential components of the velocities relative to the center of the sunspot at two different depths from August 8 data.

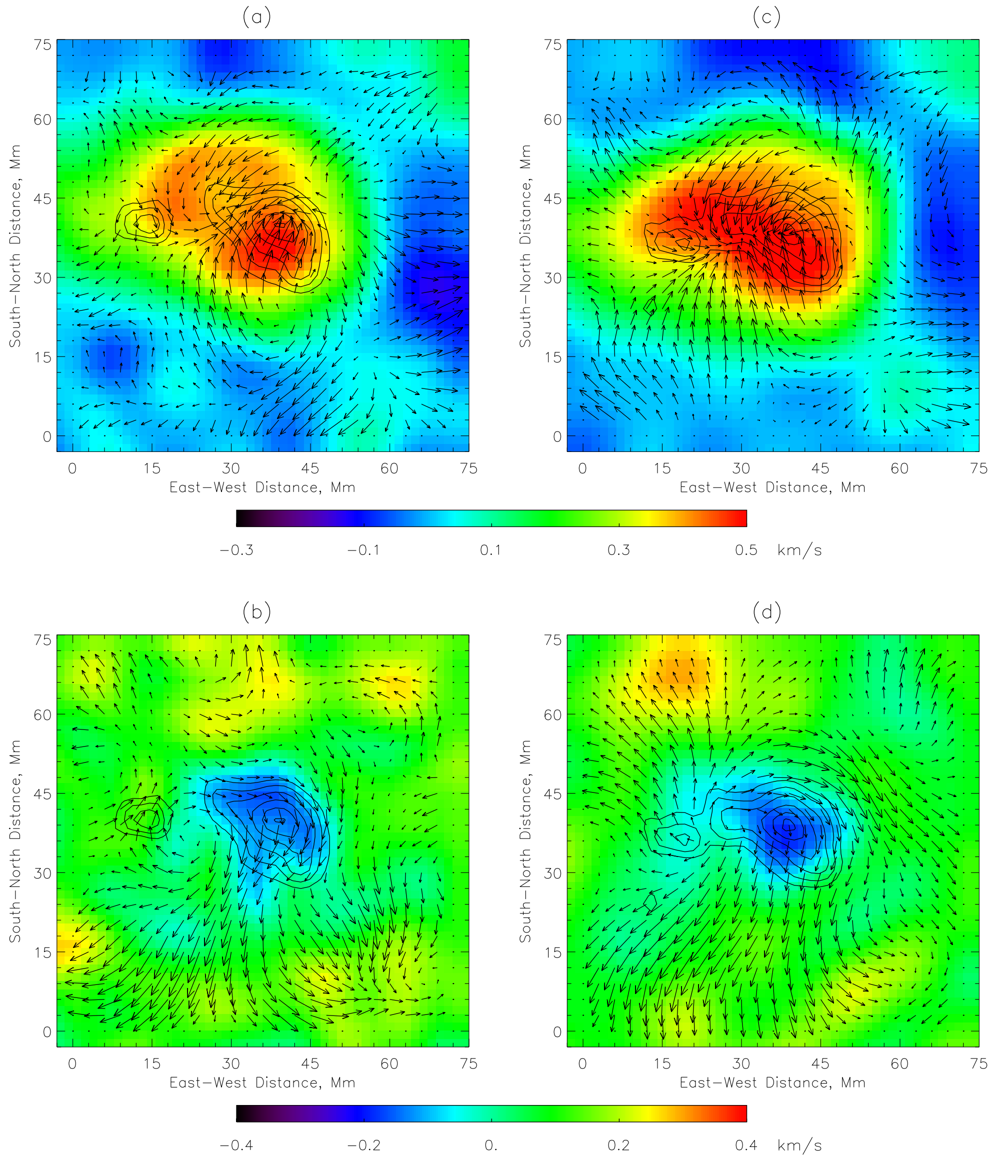

Figure 4.6: Flow fields obtained at two different depths. In the left panels, the background image shows the vertical velocities, and arrows represent the horizontal velocity field obtained from the August 7 data at the depth intervals: a) 0 – 3 Mm, and b) 9 – 12Mm. The right panels show the results for the August 8 data with same depth intervals: c) 0 – 3 Mm, and d) 9 – 12Mm. The longest arrow is 0.5 km/s for both the upper and lower graphs. The contour lines represent the line-of-sight magnetic field, the same as in Figure 4.5.

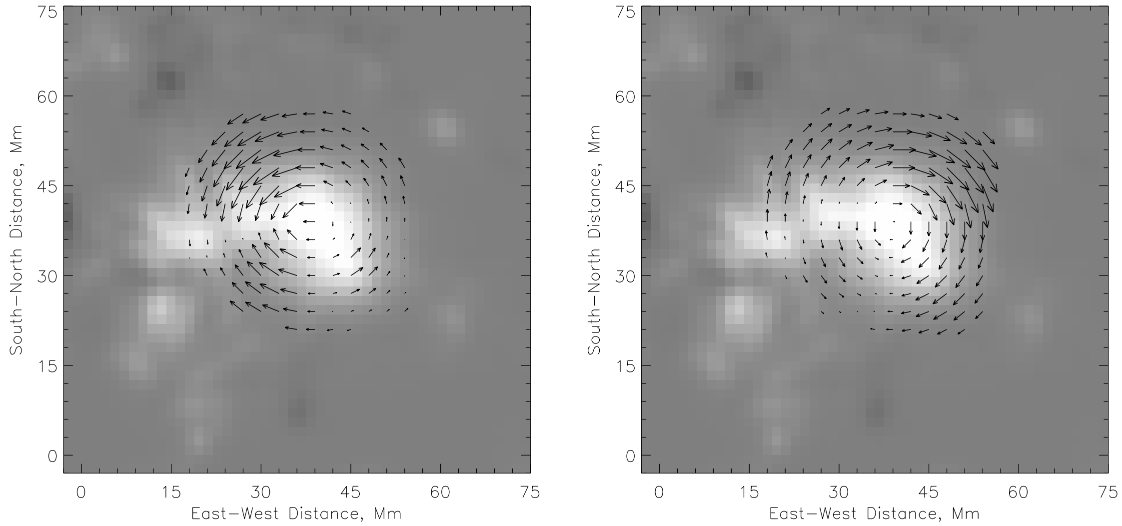

Figure 4.7: The tangential components of flow velocity relative to the center of the sunspot at two different depths 0 – 3 Mm (*left*) and 9 – 12 Mm (*right*) obtained from the August 8 data. The background images show the magnetic field same as the contour in Figure 4.5. Longest arrow in both graphs represents a speed of 0.45 km/s.

4.3.3 Kinetic Helicity

The three dimensional velocity field obtained from our time-distance helioseismic inversions enables us to estimate the kinetic helicity of the subsurface flows, which is an important characteristic quantity for solar MHD .

Following Mestel (1999), we define the kinetic helicity as

$$\alpha^v \equiv \mathbf{v} \cdot (\nabla \times \mathbf{v})/|\mathbf{v}|^2 \tag{4.1}$$

In particular, we use a component of α^v corresponding to the vertical components of velocity and vorticity:

$$\alpha_z^v = v_z(\partial v_y/\partial x - \partial v_x/\partial y)/(v_x^2 + v_y^2 + v_z^2) \tag{4.2}$$

This corresponds to the current helicity obtained from magnetograms by some previous authors, e.g., Pevtsov, Canfield, & Metcalf (1995). After computing value α_z

at each pixel, we average these values over the whole active region where $B_z > 100$ Gauss, although the selection of 100 Gauss threshold is arbitrary. The mean kinetic helicity from the August 7 velocity data (Figure 4.6a, b) is -1.01×10^{-8} m^{-1} for the depth of 0 – 3 Mm, and -2.21×10^{-8} m^{-1} for the depth of 9 – 12 Mm, and the mean kinetic helicities for August 8 data (Figure 4.6c, d) are -2.11×10^{-8} m^{-1} and -6.26×10^{-8} m^{-1}, respectively.

Based on the observations of vector magnetograms in solar active regions, Pevtsov, Canfield, & Metcalf (1995) calculated the mean current helicity of many active regions with the definition of current helicity as $\alpha = J_z/B_z$, where J_z is the line-of-sight current density and B_z is the line-of-sight magnetic field. The average kinetic helicity calculated from our inversion results of this active region has the same order of magnitude as the typical current helicity of active regions calculated by them. It is suggested by many authors (e.g., Longcope, Fisher, & Pevtsov, 1998) that the magnetic helicity observed in the photosphere may be produced by helical motions beneath the photosphere. However, we can hardly draw any conclusion about the relationship between the subsurface kinetic helicity and magnetic helicity from just one sample that we currently have. Apparently, a statistical study combining the kinetic helicity and magnetic helicity is needed for better understanding this relationship in solar active regions.

4.4 Error Analysis

4.4.1 Monte Carlo Simulation

The inverse problem of the time-distance helioseismology is reduced to the linear system $\mathbf{Ax} = \mathbf{b}$, which is solved in sense of least squares. The covariance matrix for error estimations of the inversion results is given by $C_m = \sigma_d^2(\mathbf{A}^T\mathbf{A})^{-1}$ (see Menke, 1984), where σ_d^2 is the covariance matrix from the observation data. However, it is not realistic to perform such a calculation because $(\mathbf{A}^T\mathbf{A})^{-1}$ is too large to calculate directly, and the LSQR algorithm does not give the matrix inverse explicitly, nor does the other algorithm MCD. Therefore, we estimate the error propagation by the use

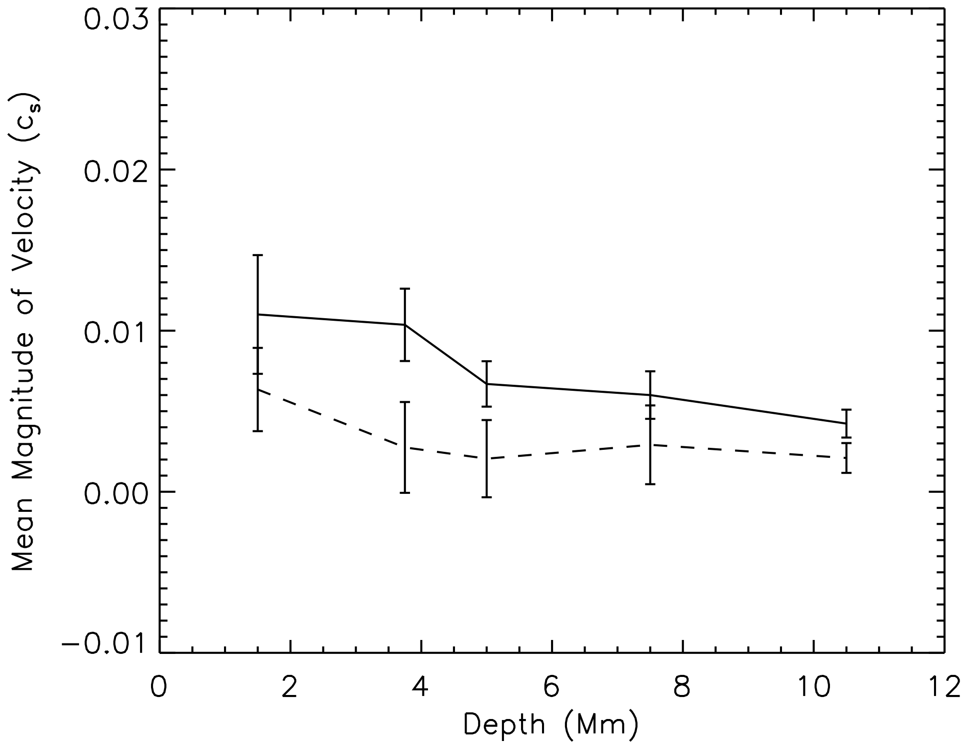

Figure 4.8: Mean magnitude of the horizontal (solid line) and vertical (dashed line) components of flow velocity at different depths with the error bars estimated by a Monte Carlo simulation. The velocities are shown in the unit of local sound-speed.

of Monte Carlo simulation.

Time-distance helioseismology calculates the wave propagation time by fitting cross-covariance of the solar oscillation signals in two locations; hence, a fitting error of the propagation time can be estimated at each pixel for different travel distances by following the description by Press et al. (1992). Typically, the fitting errors are less than 2% of the wave propagation time. However, only the travel time differences are used for the inversion, which are relatively small and therefore, have significant error levels. For larger distances, we use larger annulus intervals in which more data points are included, and in this case fitting errors are usually smaller than those from smaller distances. This is done in order to increase the reliability of the inferences for deeper layers. Then, for each specific distance, we approximate the fitting error distribution by a Gaussian function. Although the exact distribution function for the travel time fitting errors is not exactly known, to the observed distributions the Gaussian function is a good approximation.

After the distribution function of fitting errors is obtained for each distance, we perform Monte Carlo simulation by producing 40 sets of random errors consistent with the error distribution function and adding these to the travel time estimates for August 8 data. The time-distance inversion for three dimensional velocity is performed for each of these 40 datasets, respectively. After the inversion is done, the mean value and standard deviation are computed for each pixel of the velocity maps. In Figure 4.8, the average of mean values of the horizontal and vertical components of velocity are presented, and the error bars indicate the average of standard errors at different depths. We find that the results for the horizontal component of velocity are robust, while the vertical component of velocity is more uncertain (we even have difficulty in determining the correct signs at the depth from 3 to 6 Mm). However, in the depth intervals 0 – 3 and 9 – 12 Mm, which are used in our analysis of the vortical flows (shown in Figure 4.6), the errors are relatively small.

4.4.2 Umbra Mask Test

The other issue that we need to consider is the *SOHO*/MDI observation saturation problem in dark areas of sunspots umbrae (Liu & Norton, 2001), which appears in MDI magnetograms and Dopplergrams observations when the spectral line intensity drops below a certain level. Additional effect that may affect our measurements is a strong absorption of the solar acoustic power by sunspot umbrae (Braun, Duvall, & LaBonte, 1988).

In order to test how the saturation and the acoustic absorption in sunspot umbra might affect the vortical flow fields derived from our analysis, we discard all the travel times obtained inside the sunspot umbra, and then perform the inversion calculations, although only a small part of the umbra is affected by the saturation. The results are shown in Figure 4.9. We find from the masked data that at the depth of 0 – 3

Mm, the downward flow speeds are only slightly smaller than those in the original calculation, and the horizontal speeds also slightly change, but most importantly, the flow structure is not affected. We still see the same downward and converging flow patterns, thus confirming the earlier conclusion obtained in Chapter 3. Outside the sunspot umbra, the vortical flows seen in Figure 4.6 remain almost the same. At the depth of 9 – 12 Mm, the flow fields are not affected at all by the umbral mask. Therefore, we conclude that the potential uncertainties in the observations of the umbra area do not significantly affect our results.

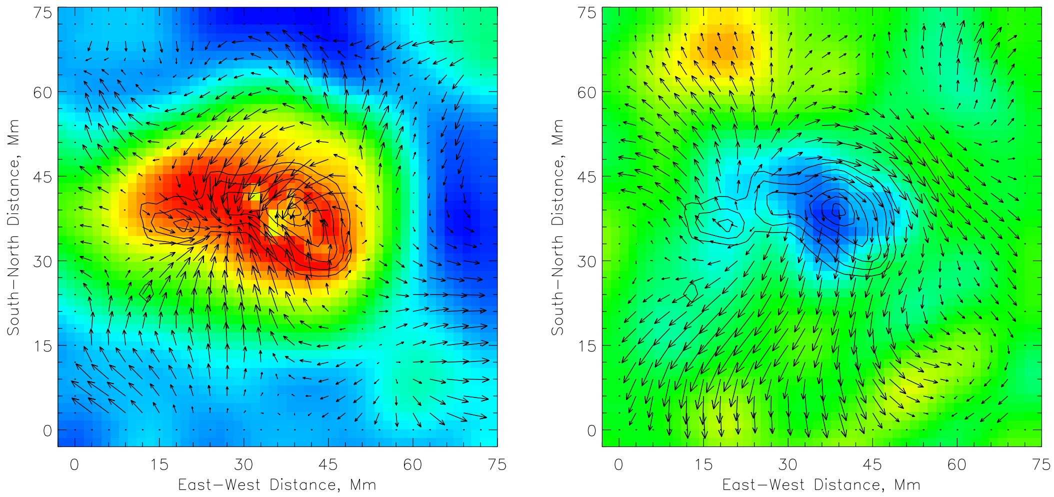

Figure 4.9: Flow fields derived for August 8 data after masking the sunspot umbra (see text). Color index and arrows are same as in Figure 4.6.

4.5 Discussion

Using the time-distance technique and inversion methods based on the ray approximation, we have mapped the sound-speed structures and flow fields beneath a rotating sunspot. We have estimated the error propagation in both the time-distance measurements and the inversion procedure by the use of Monte Carlo simulations, and found that while the vertical velocity inferences may have significant errors, estimates of the horizontal component are sufficiently robust for determination of the structure of the vortical flows. The test of masking the sunspot umbra where the measurements may be uncertain because of the observational signal saturation and wave absorption showed only slight changes in both components of the velocity in the sunspot area close to the surface and nearly no change in the deeper layers. Perhaps, the main uncertainty of our measurements comes from the ray approximation in the inversion procedure, which is known to underestimate the magnitude of perturbations, particularly at small scales (Birch et al., 2001). However, the larger scale structure of sunspots should be reproduced correctly (Jensen et al., 2001). Hence, results shown in this chapter are correct qualitatively, if not quantitatively.

Many previous observations have revealed that the magnetic field in some active regions is twisted. Evidence for the twists exhibits in various solar phenomena, such as the morphology of Hα structures (Hale, 1927), filaments (Martin, Billamoria, & Tracadas, 1994) and coronal loops (Rust & Kumar, 1996). The results presented in Figure 3 show us that the surface magnetic field of a rapidly rotating sunspot has an angle with respect to the subsurface sound-speed structure at the depth of 6 Mm. This provides observational evidence that the magnetic flux twists also exist beneath the visible surface of the active region, in addition to the previously reported twists in the solar photosphere and corona. Furthermore, it was argued that the magnetic field twists may have already formed before the emergence of magnetic flux on the surface (Leka, Canfield, & McClymont, 1996, and many other investigators). Our observation presents direct evidence that magnetic field twist may exist beneath the surface.

Assuming that the magnetic flux tubes have already been twisted below the solar surface, Magara & Longcope (2003) simulated numerically the emergence process of magnetic flux and reproduced the sigmoidal shape of coronal loops as observed in X-rays. In addition, vortical flows in and around the magnetic flux footpoints were also found in their simulations, which in turn could twist more the already twisted magnetic flux. Our observation of sunspot rotation in the photosphere and 5 Mm below the photosphere seems to be consistent with their numerical simulation for both the subsurface magnetic twists and the photospheric and subphotospheric vortical motions. Perhaps, our inference of the subsurface vortical flow fields in this study may also support the argument by López Fuentes et al. (2003) that vortical flows may exist in subphotosphere and play an important role in the formation of magnetic twists.

It is widely believed that vortical sheared flows around magnetic flux footpoints could eventually lead to solar eruptions. Recently, some authors began to calculate the energy and magnetic helicity generated by the surface flows. Some argued that the surface horizontal rotational flows could provide sufficient magnetic helicity and energy to produce solar flares (Moon et al., 2002), while others argued that magnetic helicity from subsurface must be included to be sufficient for solar eruptions (Nindos & Zhang, 2002). Our observation shows that strong subsurface vortical flows should be taken into account as a potential source of magnetic helicity and energy buildup, which can be much stronger in the deeper layers than at the surface because mass density and plasma β are much higher there.

In this study, we have found counter-clockwise vortical flows at the depth range of 0 – 3 Mm around the sunspot (which also rotated counter-clockwisely at the surface), and the evidence of reverse clockwise flows at the depth of 9 – 12 Mm. What could cause these opposite vortical flows is an open question. At present there is no theoretical model explaining the vortex motions. It may be useful to consider some analogies, for instance, it is known that for hurricanes on the Earth there are strong converging flows near the ocean surface, and divergent flows at high altitude in the atmosphere. Hence, the hurricanes have counter-clockwise flows at the bottom and clockwise flows at the top due to the Coriolis force on the Earth's northern hemisphere (e.g., Gordon, 1998). If one can think of a sunspot model as a reverse hurricane as proposed by Schatten & Mayr (1985), then the opposite vortical flows may be caused by Coriolis force. If this were the case, then magnetic flux can be twisted by these flows, hence build up a great amount of energy. However, if the reverse hurricane sunspot model is true, the question is why the vortical flows are not observed in most sunspots.

By using the time-distance inferences, we have also calculated the subsurface kinetic helicity in two different depth intervals, and obtained the kinetic helicity values of the same order of magnitude as the current helicity of typical active regions. It is reasonable to believe that kinetic helicity and magnetic helicity are related to each other in the sub-photosphere and upper convection zones, and the subsurface kinetic helicity may have some contributions to the formation of surface magnetic helicity and its hemispherical preference distribution. Certainly, how the subsurface kinetic helicity are correlated with the surface magnetic helicity needs a further statistical study. The time-distance inversion technique and results presented in this chapter enable us to carry out such study.

Further time-distance helioseismological studies of the subsurface dynamics of sunspots and active regions, particularly before powerful solar flares, may be of great importance for the investigation of the subsurface energy buildup, kinetic helicity development and their relationship with the solar eruptive events, and may lead to the possibility of solar eruptions forecast.